1

2

3

4

5

Stratified-turbulence observations in the deep Mediterranean

by Hans van Haren

Royal Netherlands Institute for Sea Research (NIOZ), P.O. Box 59, 1790 AB Den Burg,
the Netherlands.
e-mail: hans.van.haren@nioz.nl

26   **Abstract.** A nearly half-cubic hectometer of deep Mediterranean-Sea waters is yearlong sampled with

27   about 3000 high-resolution temperature sensors to study different sources of turbulent waterflows,

28   which are vital for life. Although temperature differences are never larger than 0.01°C, daily, weekly,

29   and seasonal variations are observed. About half the time, relatively warm stratified waters are moved

30   from 100's of meters higher levels to near the seafloor. These internal-wave and sub-mesoscale eddy-

31   induced motions are half an order of magnitude more turbulent than those induced via general

32   geothermal heating from below, and about one order of magnitude more turbulent than those from open-

33   ocean processes. A rough estimate shows that eddy-induced stratified turbulence is likely more

34   important for deep-sea life than rare, not observed, deep dense-water formation at the abyssal-plain

35   mooring site. With a delay of about a week, the stratified turbulence tracks atmospheric disturbances,

36   which are found 35% more energetic in winter than in summer. From comparison of turbulence-

37   calculation methods, of band-pass filtering with vertical-displacement reordering, for data over one-four

38   days, a generalization is proposed for the filter cut-offs under weakly stratified and near-homogeneous

39   conditions in the deep Mediterranean.

40

1 Introduction

41

42 Irreversible, energy-consuming turbulence is indispensable for life on earth, also in the deep sea. Most

43 ocean turbulence is generated near its boundaries, with an important input via the breaking of internal

44 waves at steeply sloping underwater topography (Eriksen, 1982; Thorpe, 1987). Observational details

45 are still scarce from the abyssal deep sea that is commonly considered to be 'quiescent and stagnant'.

46 One of the key aspects in the breaking of internal waves is the 'warming phase', when, e.g., an internal

47 tide moves downslope and characteristically (re-)stratifies waters near the seafloor with near-

48 homogeneous waters due to convection turbulence above. Less known are slantwise-moving, warm

49 turbulent waters possibly related with near-inertial waves and (sub-)mesoscale eddies in basins like the

50 Mediterranean Sea where tides and stratified conditions are both weak. As will be demonstrated in this

51 paper, these warm waters have the potential to generate larger turbulent mixing than in the open-ocean

52 interior.

53 Under weakly stratified conditions, the potential of deep-sea turbulence generation via downward or

54 slantwise moving waters should be compared with local general geothermal heating 'GH' through the

55 seafloor (e.g., Pasquale et al., 1996), and with deep dense-water formation 'DWF' from the surface (e.g.,

56 Marshall and Schott, 1999). Sparse shipborne microstructure profiling has provided estimates of

57 turbulence contributions from different sources across the Northwestern Mediterranean in which GH is

58 found more important than internal wave breaking (Ferron et al., 2017). However, details of relevant

59 processes are lacking and require high-resolution moored observations over prolonged periods of time.

60 In a stably-stratified environment like the sun-heated ocean, downward motions of warm water seem

61 impossible in relation with irreversible convection turbulence involving motion in three spatial

62 dimensions '3D'. Natural, body-forced buoyancy-driven convection (e.g., Dalziel et al., 2008; Ng et al.,

63 2016) applies to denser waters moving down and less dense waters moving up in narrow plumes, i.e. in

64 terms of temperature variations: warmer waters moving up and cooler waters moving down. In the

65 ocean, such buoyancy-driven convection turbulence occurs regularly in the upper $O(10)$ m near the

66 surface during nighttime (e.g., Brainerd and Gregg, 1995) and possibly lower 100 m above the seafloor

67 due to GH, depending on the local stratification. It can also occur as DWF after specific preconditioning

68 of stratification reduction near the surface in localized areas like polar seas and the Mediterranean during

69   brief irregular, rare periods (Marshall and Schott, 1999). An exemption can occur when the other major

70   contributor to density variations dominates over temperature variations: if downward moving warm

71   waters are sufficiently saltier than there environment, cooler and fresher waters may move up.

72   A reversible, also 3D, process occurs when internal-wave motions affect the stratified environment

73   (e.g., LeBlond and Mysak, 1978). Such motions may displace relatively warm waters downward during

74   a particular wave-phase, and cooler waters up. However, such displacements will not overturn and

75   vertically mix the different water masses.

76   A combination of irreversible and reversible processes was observed in fresh-water alpine Lake

77   Garda, where in the weakly stratified waters underneath internal waves convection turbulence was

78   observed (van Haren and Dijkstra, 2021). As these observations showed similarity with the warming

79   phase of a nonlinear wave breaking above a sloping seafloor (e.g., van Haren and Gostiaux, 2012), it

80   was suggested that the convection underneath internal waves was either generated via shear moving

81   convection tubes slantwise, or via wave-accelerations overcoming vertical density differences in

82   internal-forcing overcoming reduced gravity, instead of body-forcing overcoming gravity as in natural

83   convection. Similar to the effect of large-scale shear, planetary slantwise convection in the direction of

84   the Earth's rotational vector may be brought about by the horizontal Coriolis parameter f_h (Marshall and

85   Schott, 1999). The convection can be induced via resonantly-forced standing inertial waves under

86   homogeneous conditions (McEwan, 1973). At mid-latitudes, apparently-stable stratification having

87   buoyancy frequencies of $N = f_h$, $2f_h$ or $4f_h$ occur in marginal stability due to planetary slantwise

88   convection (van Haren, 2008).

89   In this paper, we further pursue the investigation of downward convective warm-water periods

90   inducing stratified-turbulence that occur frequently in the deep Western Mediterranean. For this

91   purpose, a nearly half-cubic-hectometer large 3D mooring-array is constructed holding about 3000 high-

92   resolution temperature T-sensors and deployed at a deep seafloor. Turbulence calculations are made for

93   a full observational year to investigate potential seasonal variations. Of the governing physics processes

94   that indirectly may affect deep-sea life by inducing or transporting sufficient turbulence for nutrient and

95   oxygen supply are: atmospheric-disturbance generated near-inertial waves, boundary-flow instability

96   generating sub-, O(1) km, and meso-, O(10-100) km, scale eddies. Motions associated with these

97 processes dominate dispersal of water masses in seas and oceans. While they are not considered to be

98 part of irreversible 'small-scale' turbulent mixing, they are all greatly affected by the rotation of the

99 Earth. How they transfer energy to small-scales of turbulence dissipation is not yet fully established.

100 The large number of independent T-sensors is expected to improve statistics of turbulence values, in an

101 environment where all dynamics is captured by temperature variations of less than 0.01°C. The small

102 temperature variations put a large strain on the technical capabilities of quantifying the deep-sea

103 turbulence.

104

105 **2 Materials and Methods**

106   In order to get some insight in the generation and development of deep-sea turbulence, 2925

107 independent, self-contained high-resolution NIOZ4 temperature 'T'-sensors were distributed in nearly

108 half-a-million cubic meters of seawater. With two supplementary T-sensors registering tilt information

109 above and below, 63 T-sensors were taped at 2-m intervals to 45 vertical lines 125-m tall that each were

110 tensioned to 1.3 kN by a single buoy on top. The T-sensors were located between nominally h = 1.5-

111 125.5±0.5 m above seafloor and recorded data at a rate of once per 2 s. Three buoys, of lines 1.4, 3.5

112 and 5.7 (henceforth throughout the text, the original naming 'group.line' is shortened without period;

113 for layout see Appendix A1), held a single-point Nortek AquaDopp current meter 'CM' at h =126 m,

114 which recorded data once per 600 s. The lines were attached at 9.5-m horizontal intervals to a steel-

115 cable grid that was tensioned inside a 70-m diameter steel-tube ring functioning as a 140-kN anchor.

116 The ensemble 'large-ring mooring' was deployed on the <1° flat and 2458-m deep seafloor of 42°

117 49.50′N, 006° 11.78′E just 10 km south of the steep continental slope, 5 km from its abyssal-plain foot,

118 of the Northwestern Mediterranean Sea, in October 2020 (Fig. 1a). At the site's (mid-)latitude f_h = 1.08f.

119 Details of construction and deployment of the large-ring mooring can be found in van Haren et al.

120 (2021). For calibration and reference purposes, a single shipborne Conductivity Temperature Depth

121 'CTD' profile was obtained to h = 0.5 m, about 1 km horizontally from the mooring site during the

122 deployment cruise.

123   With the aid of Irish Marine Institute Remotely Operated Vehicle (ROV) "Holland I" all 45 vertical

124   lines with T-sensors were successfully recovered in March 2024. Of the lines, 43 were mechanically in

125   good order. Line 18 was hit by the drag parachute, which functioned as a stabiliser during the free-fall

126   deployment, whereby 10 sensors were lost. Line 65 was about 0.5-m lower than nominal because of a

127   loop near the cable grid. Fig. A1 shows the numbering of the lines, which were ordered in six groups

128   for synchronisation purposes. As with previously deployed NIOZ4 T-sensors (for details see van Haren,

129   2018), the individual clocks were synchronised to a single standard clock every 4 hours, so that all T-

130   sensors were sampled within 0.02 s. Line 36 did not register synchronization, possibly due to an electric

131   cable failure. Three T-sensors leaked and <10 were shifted in position due to a tape malfunctioning.

132   After calibration, some 20 extra T-sensors are not further considered due to electronics (noise) problems.

133   In total, 2882 out of 2925 T-sensors functioned as expected for the first 20 months after deployment,

134   with remaining bias due to electronic drift resulting in deviations from absolute accuracy. Depending

135   on the period and type of analysis considered, between 50 and 150 T-sensors showed too large bias

136   requiring additional attention during post-processing of the records from the weakly stratified deep sea.

137   Due to unknown causes all T-sensors switched off unintentionally when the file size on the memory

138   card reached 30 MB. This may have to do with a formatting or programming error. It implied that a

139   maximum of 20 months of data was obtained.

140   With respect to previous NIOZ4 T-sensor version, improvements of the electronics resulted in about

141   twice lower noise levels of 0.00003°C and twice longer battery life. As described in van Haren (2018),

142   calibration yielded a relative precision of <0.001°C. Bias due to instrumental electronic drift of <

143       $0.001°C \text{ mo}^{-1}$ after aging was primarily corrected by referencing daily averaged vertical profiles, which

144   must be stable from a perspective of turbulent overturning in a stratified environment, to a smooth

145   polynomial without instabilities. In addition, because vertical temperature (density) gradients are so

146   small in the deep Mediterranean, reference was made to periods of typically one hour duration that were

147   homogeneous with temperature variations smaller than instrumental noise level (van Haren, 2022). Such

148   periods were on days 350, 453, and 657 in the existing records. This secondary correction included low-

149   pass noise filtering 'lpf' of data with time. Under near-homogeneous conditions, a tertiary correction

150   involved lpf of data in the vertical. Temperature records were pressure-corrected by transferring to

151   Conservative Temperature Θ (IOC et al., 2010) using CTD's mean local salinity value. Henceforth, Θ

152   will be named 'temperature', for short.

153   Given the consistent and tight temperature-density relationship (Section 3), corrected temperature

154   data allowed for calculations of turbulence values using the overturning displacement method of Thorpe

155   (1977) by reordering density instabilities. Here, the method is applied under weakly stratified conditions

156   in which buoyancy frequency $N \ll 10f$, f denotes the local inertial frequency. For the present deep-sea

157   area, distinction is made between periods under environmental conditions when $N \sim> f$, somewhat

158   exaggerating named stratified-water 'SW' conditions, and $N \sim< f$ including unstable values, named near-

159   homogeneous 'NH' conditions. For NH, the tertiary correction is needed, and, when unstable overturns

160   exceed the 124-m vertical range of sensors, an extra correction is mandatory because the Thorpe (1977)

161   method of reordering is over-estimating displacements and resulting stratification (van Haren, 2025).

162   Such periods are difficult to trace, because of the extremely small vertical temperature differences, and

163   the selection can only be done manually as it is inadequately automated.

164   For comparison with mean Thorpe (1977) method, turbulence values are also computed using

165   'Ellison'-scales (Ellison, 1957 for atmospheric data; Itsweire, 1984 for laboratory data; Moum, 1996 for

166   oceanographic microstructure profiler data). Such scales are determined from moored T-sensor time

167   series by filtering out internal wave and sub-mesoscale motions. The method is quite sensitive for the

168   precise high-pass filter 'hpf' cut-off frequency, as was noted for well-stratified Atlantic Ocean waters

169   (Cimatoribus et al., 2014 for oceanographic moored T-sensor data). Here in Appendix A2, a modified

170   version for application to moored T-sensor data under very weakly stratified conditions is proposed and

171   filter cut-off frequencies are given for SW and NH conditions in the deep Mediterranean. For both

172   methods, mean values are obtained from moored multiple-line T-sensor records after averaging over at

173   least the largest turbulence scales, over the vertical '[…]', over time '<…>', and over 45 horizontally

174   distributed lines '(…)'.

175

176

177

178   **3 Results**

179   The focus is on the first full year of observations to investigate potential seasonal variation in deep-sea

180   turbulence values. The yearlong data-overview time series in Fig. 2 demonstrates 2-30 day variations,

181   in waterflow speed (Fig. 2a), temperature (Fig. 2b), horizontal velocity difference (Fig. 2c), and vertical

182   temperature difference (Fig. 2d). Such time-variability is typical for sub-meso- and mesoscale motions,

183   which are likely associated with the dynamically unstable, meandering boundary current over the

184   canyon-incised steep continental slope (Crepon et al., 1982) and which may develop into eddies.

185   Over the one year of observations, the waterflow speed U seldom exceeds 0.1 m s^{-1}, with little

186   variations through the seasons. U also rather strongly varies with local inertial period, which partially

187   reflects the variable thickness of the graphical curves in Fig. 2a.

188   Inertial motions do not dominate T-sensor data (Fig. 2b,d). Also in contrast with U, the T-data

189   demonstrate a seasonal variation with relatively warmer (Fig. 2b) and more stratified (Fig. 2d) waters in

190   winter, coarsely between days 365 and 495. The entire dynamical temperature variation over the year

191   and up to h = 125 m from the seafloor is captured within maximum $|\Delta\Theta| < 0.01$°C, and commonly

192   amounts only a few millidegrees. About half the time, $\Delta\Theta > 0.0002$°C $\equiv T_{thres}$, a threshold level that is

193   about ssix times the standard deviation of T-sensor noise level and which provides an overall

194   stratification resulting in N > 0.65f. These relatively warm SW either come from above or from the side.

195   The other half of the time $\Delta\Theta < T_{thres}$, N < 0.65f and stratification may be unstable, or NH conditions.

196   Under NH, less than 0.7% of total time negative temperature differences are found exceeding the

197   (absolute value of) threshold level and corresponding with large-scale, >125-m developed GH. As a

198   result, at the observational site convection turbulence associated with GH is suppressed by warm waters

199   advected into the area most of the time.

200   Although the boundary current is strongest near the surface, it manifests itself at great depths

201   including mesoscale variations at horizontal scales O(10-100) km. However, observed spatial waterflow

202   variations over about 50-m horizontally indicate much smaller-scale, rapidly-fluctuating differences

203   (Fig. 2c). These variations associate, in absolute value, with warm SW conditions in approximately half

204   the cases. No cooling, inversely stratified waters, from above are observed in the yearlong record.

205   Compared to open-ocean waters where large 100-m scale N > 10f, the deep Mediterranean SW are

206   characterized by weak stratification with N = O(f). Despite the relatively weak stratification, SW will

207   prove important for turbulent mixing in the area.

208   The single shipborne CTD observations show no dominant influence of salinity over temperature

209   governing density variations, in the lower 500 m above the seafloor (Fig. 3). Over the well-resolved

210   stratified portion between -2165 < z < -2055 m, the density-temperature relationship is found to be

211   consistent (cf. van Haren, 2025),

212    $\delta\sigma_2/\delta\Theta = -0.25\pm0.01$ kg m^{-3} °C^{-1},   (1)

213   where $\delta\sigma_2$ denotes the density anomaly referenced to a pressure level of 2×10^7 Pa. Hence, Θ can be used

214   as tracer for density variations to quantify turbulent overturning using the Thorpe (1977) method.

215   In the weakly stratified waters over a vertical range of 100 m, density stratification varies, so that N

216   < 1f or NH is found near the seafloor, and N ≈ 2f or SW around z = -2050 m (Fig. 3d). Over 25-m

217   vertical ranges, N ≥ 2f can be found (Fig. 3d), and over 1-10 m ranges N > 4f may be inferred from Fig.

218   3c around z = -2110 and -1980 m. Such thin stratified layers are occasionally also found at greater depths

219   if the better-resolved temperature profile is investigated (Fig. 3b). While the occasional vertical

220   temperature differences of <0.01°C in Fig. 2d could result from horizontal differences or fronts, it seems

221   more likely that stratification of around z = -2050 m in Fig. 3 is periodically lowered by action from

222   above. Such action is expected down to about h < 10 m from the seafloor, a thin layer in which vertical

223   temperature differences are generally very small but not always (black graph in Fig. 2d).

224   Thus, although the moored T-sensors were located between the seafloor and z = -2332 m, CTD-

225   measured stratification may vary considerably with depth and time, and physical processes may lower

226   warmer water some 400 m or advecting such waters slantwise, or possibly quasi-horizontally into the

227   range of T-sensors. The precise direction of warm-water motion cannot be determined from single-

228   station profiles, but may be resolved with a properly scaled 3D mooring-array.

229

230

231

232 **3.1 1D-details of an arbitrary warm-water period**

233 Considering an average 5-mK-amplitude warm-water period (cf. Fig. 2b), a 1.3-day depth-time detail

234 from around day 485 is presented from single line 15 (Fig. 4). While waters seem depressed from h >

235 125 m, the warming occurs in variable periods of <1 hour (Fig. 4a). During the second half of the

236 warming, 0.001°C additional heat is observed near the top. Relatively warm waters reach the seafloor

237 twice within an inertial period of 0.73 day, around days 485.45 and 485.80. The warming ends with two

238 cooler-water fronts and large overturning reaching the seafloor around day 486.2.

239 The warming is depressed to within h < 10 m from the seafloor, with a relatively large vertical

240 temperature gradient between the cooler waters near the seafloor and the warmer waters higher up. This

241 is reflected in the increased value of 2-m-small-scale buoyancy frequency N_s in h < 30 m. Turbulent

242 overturns hardly occur between days 485.2 and 486.15 for h < 5 m, but are non-negligible in the stratified

243 waters above for 5 < h < 30 m, and are typically 50-m large further up for h > 30 m (Fig. 4b).

244 Quantifying turbulence dissipation rate requires averaging, over all overturning scales possible, and

245 124-m vertically averaged values demonstrate variations with time over two orders of magnitude, when

246 reordered data are used (Thorpe (1977) method, black graph in Fig. 4c), or using 48 < ω < 3000 cpd

247 (cycles per day) band-pass filtered data (Ellison (1957) method cf. Appendix A2, cyan graph in Fig. 4c).

248 Time-depth mean values for line 15 from SW's day 485 are: turbulence dissipation rate $<[\varepsilon_T]>$ =

249 $6\pm3\times10^{-10}$ m^{2}s^{-3} and turbulent diffusivity $<[K_z]>$ = $1.5\pm0.7\times10^{-3}$ m^{2}s^{-1} under buoyancy frequency $<[N]>$

250 = $2.9\pm0.3\times10^{-4}$ s$^{-1} \approx$ 3f, using Thorpe (1977) method. Modified Ellison (1957)-method $<[\varepsilon_E]>$ = $7\pm3\times10^{-10}$

251 ^{10} m^{2}s^{-3} (Appendix A2). These turbulence values are more than one order of magnitude larger than open-

252 ocean values observed in stratified waters well away from boundaries (e.g., Gregg, 1989; Polzin et al.,

253 1997; Yasuda et al., 2021).

254

255 **3.2 1D-details of an arbitrary near-homogeneous period**

256 For comparison, such turbulence values are under NH conditions between days 316.5 and 320.5 (Fig.

257 5): $2\pm1\times10^{-10}$ m^{2}s^{-3} and $1.1\pm0.5\times10^{-2}$ m^{2}s^{-1} under buoyancy frequency $<[N]>$ = $0.5\pm0.2\times10^{-4}$ s^{-1} = 0.5f.

258 These values follow partially correcting the original method by Thorpe (1977) for overturns exceeding

259 the height of instrumentation with information from manually selected NH environments that are

260　bounded by stratification above (van Haren, 2025). For periods with NH bounded by stratification

261　above, such as between days 318.6 and 318.96, their mean turbulence dissipation rate is to within 10%

262　the same as found for periods with convection turbulence due to GH: $\varepsilon_{GH} = 1.2\times10^{-10}$ m^{2}s^{-3}. The ε_{GH}

263　matches average geophysical heat-flux observations in the area (Pasquale et al., 1996), under the

264　condition that the mixing coefficient of $\Gamma_C = 0.5$ (van Haren, 2025), which is typical for buoyancy-

265　driven convection turbulence (Dalziel et al., 2008). For this period, $<[\varepsilon_E]> = 1.3\pm1\times10^{-10}$ m^{2}s^{-3}

266　(Appendix A2).

267

268　**3.3 Some 45-line statistics of short periods under SW and NH conditions**

269　For consistency and statistics, six half-day periods are considered for computation of turbulence

270　dissipation rate values, three under SW and three under NH conditions. The computations are performed

271　for all 45 vertical lines and averages are computed over the 124-m height and half-day periods. It

272　provides a one-and-a-half order of magnitude distribution of mean turbulence dissipation rate values

273　(Fig. 6).

274　　While some values are highly consistent between lines, e.g. the most energetic period on day 441,

275　others show a half-order of magnitude distribution of values like on day 459. Initially, this calculation

276　was set-up to help identify biased T-sensors and the appropriate polynomial correction. After applied

277　tertiary correction, remaining wide distributions are attributed to more general turbulence variability.

278　　The statistics certainly improve turbulence dissipation rate values calculated using other

279　instrumentation and methodology, which is generally to within a factor of two at best. The six examples

280　of 45 lines provide about four times better statistics for the half-day periods (Table 1). The three NH

281　values average to $<[\varepsilon_T]>_{NH} = 1.1\pm0.2\times10^{-10}$ m^{2}s^{-3}, which is well within error equivalent to ε_{GH} for $\Gamma_C =$

282　0.5, while significantly different from the value for $\Gamma_C = 0.2$. It thus confirms previous results (van

283　Haren, 2025) and laboratory findings for convection-turbulence (e.g., Dalziel et al., 2008). The three

284　SW values average to $<[\varepsilon_T]>_{SW} = 8\pm5\times10^{-10}$ m^{2}s^{-3}, noting that the standard deviation of individual mean

285　values are one order of magnitude smaller.

286   Another consequence of the use of multiple mooring lines besides improved statistics, is some insight

287   in possible distribution of mean turbulence values. While one would expect erratic distribution over the

288   short horizontal distances <70 m, particularly NH distributions yield two-dimensional consistent images

289   such as on days 459 and 495 (Fig. 7). It provides confidence in consistency of methods used, but results

290   in a puzzling gradient in turbulence that apparently is independent of waterflow (measured at h = 126

291   m). For these GH- and near-inertial eddies-dominated periods the 9.5-m interval between lines seems

292   reasonably well chosen, where 100 m may have been too large.

293

294   **3.4 Yearlong daily averaged turbulence for 45 lines**

295   A yearlong time series of daily-averaged turbulence values is computed for all 45 lines (Fig. 8). This

296   computation is automated, using a fixed 3rd-order polynomial for primary correction. Since the tertiary

297   correction for >125-m extending overturns is not applied manually, a criterion for excluding such

298   episodes is applied. The criterion is simply based on the daily-averaged temperature difference between

299   uppermost and lowest T-sensor, per line. When $\Delta\Theta < T_{thres}$, given previously, the daily and vertical mean

300   dissipation rate is fixed to,

301        $<[\varepsilon_T]> = \varepsilon_{GH} = 1.2\times10^{-10} \text{ m}^2 \text{ s}^{-3}$,   (3)

302   the mean value for geothermal heating (van Haren, 2025). This is found to occur in 59±1.5% of the time,

303   somewhat varying per line, and characterizes NH, besides GH. About 40±1.5% of the time is

304   characterized by SW.

305   The overall, yearlong, 125-m vertical, and 45-line mean turbulence dissipation rate amounts,

306        $(<[\varepsilon_T]>) = 2.4\pm0.2\times10^{-10} \text{ m}^2 \text{ s}^{-3}$,   (4)

307   so that the mean SW turbulence dissipation rate amounts,

308        $(<[\varepsilon_T]>)_{sw} = 4.3\pm0.4\times10^{-10} \text{ m}^2 \text{ s}^{-3}$,   (5)

309   which is thus closely represented by the short periods of days 308 and 485 in Fig. 6, Table 1.

310   Part of the SW-turbulence is attributable to GH in a layer of typically h = 30 m under stratified waters.

311   This may be inferred from the vertical temperature difference in that layer that passes T_{thres} during only

312   8% of daily periods, cf. the magenta graph in Fig. 2d. Nevertheless, the advection of warmer waters

313 suppresses GH-turbulence, possibly affecting the small-scale distribution in Fig. 7, and the associated

314 3.5-times larger turbulence dissipation rates (5) are induced by convection and more generally by shear

315 following internal-wave breaking.

316   Considering the yearlong 'seasonal' variation that was suggested from the temperature (difference)

317 time series in Fig. 2, and which is represented by the logarithm of daily and vertically averaged $<[N]>$

318 in Fig. 8c, the corresponding plot of $<[\varepsilon_T]>$ (Fig. 8b) is more difficult to interpret, also in conjunction

319 with meteorological data (Fig. 8a). Different-line data mostly collapse on each other during winter

320 between days 365 and 495, for both $<[N]>$ and $<[\varepsilon_T]>$. During this period, vertical-line daily mean

321 turbulence dissipation rates most, 27 out of 41, exceed twice the mean value (4), shown by the green

322 asterisks in Fig. 8a. The 11% of time of green-asterisks occurrence average to a mean turbulence

323 dissipation rate of 7×10^{-10} m^2 s^{-3}.

324   The average turbulence dissipation rate for the 130-day winter period is 25% higher than the yearlong

325 mean (4). During this period, the wind work $\sim W^2$ is increased by 20% compared to its yearlong average

326 value. A rough visual correspondence is found between $|W|$ (Fig. 8a) and $\lg<[\varepsilon_T]>$ (Fig. 8b), the former

327 leading the latter by about one week. The clearest value-collapse of turbulence and stratification data

328 from different lines is found between days 450 and 500. The early-spring period is unlikely governed

329 by deep DWF due to limited meteorological forcing (Fig. 8a), but the preceding winter cooling may

330 induce enhanced sub-mesoscale activity. Although increased sub-mesoscale motions can obscure near-

331 inertial internal waves (van Haren and Millot, 2003), the transfer of energy to internal-wave scales

332 leading to breaking and turbulence is not hampered. Possibly, as near-inertial shear is dominant in well-

333 stratified waters, a shift from shear to convection turbulence may be associated with the increase of sub-

334 mesoscale activity. Such potential energy transfer will be elaborated elsewhere.

335   In contrast, 14% lower mean turbulence dissipation rate than (4) is found during the summer between

336 days 540-670. In this period, W^2 is decreased by 13% compared to its yearlong average value.

337

338

339

4 Discussion and conclusions

The observations show short O(10) day periods of typically 0.005°C warmer waters than their environment appearing from above, but also, as inferred from the 3D mooring-array, from the sides. The periods occur at a coarse near-inertial periodicity, which is much less deterministic than a tide, and at twice the inertial periodicity. Like internal waves in the Atlantic and Lake Garda (van Haren and Dijkstra, 2021), they push stratification to within a few meters from the seafloor. The pushdown is vigorously turbulent, more than one order of magnitude larger than in the open ocean away from boundaries. This relatively large turbulence should not surprise as both the bulk Reynolds number $O(10^6)$ and buoyancy Reynolds number $\varepsilon/(\nu N^2) = O(10^4)$ are large, even in the weakly stratified deep sea. The $\nu \approx 10^{-6}$ m^2 s^{-1} denotes the kinematic viscosity. As GH is found to be relatively weaker, the convection turbulence seems to be driven by the, slanted, internal waves from above.

While vertical motions by wintertime DWF have been observed via moored observations (e.g., Schott et al., 1996) and floats (Steffen and D'Asaro, 2002), and surface buoyancy fluxes have been estimated to be $O(10^{-7})$ m^2 s^{-3} during convection events (Marshall and Schott, 1999), quantification via observations of turbulence values associated with DWF reaching the abyssal seafloor have yet to be made (Thorpe, 2005). Unfortunately, a dense-water event never reached the large-ring mooring while it was underwater. Estimates of deep-convection duration are limited, albeit that some consensus exists about decadal variability or occurrence of seafloor-reaching DWF over a relatively short period of (less than) a week (Lilly et al., 1999), maximum a month, per 8-10 years (Dickson et al., 1996; Mertens and Schott, 1998). It is tempting to compare coarse DWF turbulence estimates with GH and SW turbulence calculated from observations at the present mooring site.

Because of the lack of measurements to quantify DWF turbulence, some insight is gained from nocturnal convection-turbulence near the ocean surface. Microstructure measurements by, e.g., Brainerd and Gregg (1995) demonstrated turbulence dissipation rate values $> 10^{-7}$ m^2 s^{-3} close to the surface and which decreased in the O(10) m near-homogeneous layer to typically,

$$\varepsilon_{\text{DWF}} \approx 10^{-8} \text{ m}^2 \text{ s}^{-3}, \tag{6}$$

366   at a depth just above well-stratified waters below. The one order of magnitude reduced value reflects

367   the erosion of the stratification. Here, we take value (6) as a proxy for dissipation rate by an event of

368   DWF-convection turbulence in waters just above the deep seafloor.

369   In comparison with GH's value (3), DWF's (6) is two orders of magnitude larger. Where GH is

370   quasi-permanent, DWF rarely occurs, for example not at all during the presented 20 months of

371   observations. Two orders of magnitude difference implies occurrence of (6) during one month per 8

372   years to match (3). This is the estimated maximum at a given site.

373   In comparison with mainly sub-mesoscale and internal-wave induced year-average value (4), DWF's

374   (6) would have to occur during 2.5 months per 8 years, or during 9 days every year. This is not observed

375   in the open Liguro-Provençal basin. It implies that, either DWF turbulence is stronger than (6) also for

376   z < -2000 m, which seems unlikely, or GH turbulence and especially SW turbulence are several times,

377   SW turbulence up to one order of magnitude, larger than DWF turbulence, when averaged over a decade

378   in time. With their sources of sub-mesoscale eddies and near-inertial waves, the warm SW conditions

379   thus seem more important than DWF for supply of fresh materials in the deep-sea area. Recall that the

380   observations are made in an area where tides, normally about half the ocean's mechanical energy source,

381   are weak.

382   The observed yearlong mean turbulence dissipation rate value of SW being 2.5 times that of GH in

383   the present area is the reverse of findings by Ferron et al. (2017), who find three times larger GH than

384   SW from sparse microstructure profiling across the entire Northwest Mediterranean. The discrepancy

385   may have to do with the location of the large-ring mooring, about 5 km from the foot of the continental

386   slope and most likely under the well-stratified boundary current most of the time.

387   Estimating turbulence dissipation rates from the microstructure profiler plots in Ferron et al. (2017)

388   gives average values for h = 100-600 m (the instruments were stopped some 90 m above the seafloor)

389   of about 2.5×10^{-10} m^2 s^{-3} and 7×10^{-10} m^2 s^{-3}, for the Western Mediterranean and specifically Ligurian

390   Sea, respectively. These values are in the same range as mean and SW values (4) and (5), respectively.

391   Both averaged microstructure profiles showed reduction in values in the lower h = 100-200 m to about

392   1×10^{-10} m^2 s^{-3} and 3×10^{-10} m^2 s^{-3}, respectively. For properly processed microstructure profiler data the

393   instrumental error is to within a factor of two for mean turbulence dissipation rate values, not considering

15

394 environmental variations. The shown values, from the same height above seafloor as the upper range of

395 the moored T-sensors, compare with the GH-(3) and mean-(4) values determined at the large-ring

396 mooring.

397   A contribution of salt to density variations may possibly affect the turbulence values calculated from

398 the moored T-sensors under SW conditions, but density-temperature relationship across stratified layers

399 is found consistent between different years (van Haren, 2025). Also, convection turbulence under SW

400 conditions has been observed in deep alpine-lake Garda where salt contributes little to density variations

401 (van Haren and Dijkstra, 2021).

402   The relative importance of stratified turbulence occurring in varying strength over about half the time

403 has consequences for deep-sea transport, redistribution of matter and life. The regular replenishment is

404 partially related with atmospheric disturbances, in an indirect way. Winds do not directly affect motions

405 near the 2500-m deep seafloor. However, wind-induced near-inertial internal waves and boundary-

406 current variations affecting sub-mesoscale eddies seem to have correspondence with turbulence intensity

407 variations close to the seafloor, roughly a week after variations occur near the surface. More SW activity

408 and about 20% larger turbulence dissipation rates were found in winter when atmospheric activity was

409 correspondingly larger. Weakest stratification was found more in summer. As eddies and near-inertial

410 waves cause convection in the direction of the rotational axis to slant to the vertical under weak z-

411 direction stratification $N = O(f)$, cf. McEwan (1973); Straneo et al. (2002); Sheremet (2004); Gerkema

412 et al. (2008), the turbulence may come from above and in part horizontally.

413   In between stratified turbulence periods, waters tend to become near-homogeneous whilst being

414 dominantly mixed by convection turbulence through GH. As in Rayleigh-Taylor convection, plumes of

415 GH-response in waters overlying the seafloor strongly vary with time, and thus spatially (e.g., Dalziel

416 et al. 2008; Ng et al., 2016).

417   Geologically, even over a nearly flat sedimented seafloor underlying crustal cracks may develop

418 variable GH over distances as small as <1 km, depending on location of faults (e.g., Kunath et al., 2021).

419 This could explain observed variation in mean turbulence dissipation rates over the 70-m size of the

420 large-ring mooring, during GH. The 0.6-m high steel tubes of the large ring will not affect GH up to h

421 = 125 m. An inconclusive variation of mean turbulence values over periods of SW conditions

422 demonstrates larger scale variability.

423   Overall, the 45 vertical lines and nearly 3000 high-resolution T-sensors provided improved statistics

424 for daily mean turbulence dissipation rate values to within a reduced relative error of about 25%. Other

425 strengths of the mooring-array like improved spectral resolution and 3D evolution of turbulence will be

426 reported elsewhere, while short movies of 3D turbulence passages have been described in van Haren et

427 al. (2026).

428

429 *Data availability.* Only raw data are stored from the T-sensor mooring-array. Analyses proceed via

430 extensive post-processing, including manual checks, which are adapted to the specific analysis task.

431 Because of the complex processing the raw data from the custom-made T-sensors are not made publicly

432 accessible. Current meter and CTD data are available from van Haren (2025): "Large-ring mooring

433 current meter and CTD data", Mendeley Data, V1, https://doi.org/10.17632/f8kfwcvtdn.1. Atmospheric

434 data are retrieved from https://content.meteoblue.com/en/business-solutions/weather-apis/dataset-api.

435

436 *Competing interests.* The author has no competing interests.

437

445

Appendix A1 Layout of large-ring mooring

446

447 The large-ring mooring has a diameter of nearly 70 m (Fig. A1). The eighteen 12-m long and 0.6-m

448 diameter steel tubes hold a steel-cable grid for rigidness. The cables are 9.5 m apart. At cable-intersects,

449 2.5-m diameter 'small' rings are mounted that each held a 125-m long mooring line with 65 T-sensors

450 below a single 1.45-kN buoy. Of eight small rings, imaginary intersects were at the steel tubes, so that

451 special off-set mounting was needed with three assist cables (van Haren et al., 2021). Upon landing at

452 the seafloor following parachute-controlled 'free' fall, the orientation of the ring was directed to the

453 NNW, pointing at 337 °N. After underwater chemical release of the buoys, the cable-grid was lifted in

454 a dome with its center h = 2.0 m above seafloor (van Haren, 2026 submitted).

455 The vertical mooring lines were named in six synchronisation groups, of maximum eight lines each.

456 The single synchroniser was located at the small ring of central line 51. Every half hour, the synchroniser

457 sent a clock pulse to a group. The synchronisation sequence of six pulses was repeated every four hours.

458

459 **Appendix A2 Proposed generalization of filter cut-off to compute Ellison scales**

460 Data from moored strings of high-resolution temperature sensors are potentially useful to compare two

461 different manners of calculating turbulence values. The more common method proposed by Thorpe

462 (1977) involves the reordering or sorting of unstable density overturns and the bookkeeping of their

463 vertical displacements, for vertical profiles at each time step. Turbulence values are computed following

464 averaging in the vertical, in time, or both and should include the largest of overturn scales. The method

465 requires a consistent temperature-density relationship. In near-homogeneous waters, difficulties may

466 arise in establishing such a relationship, but also in determining the size of largest overturns when they

467 outgrow the height of the string. A method is proposed to correct over-estimation under convection

468 turbulence by GH using verification via results from geophysical sampling (van Haren, 2025). In well

469 stratified waters, the Thorpe (1977) method has been successfully compared (e.g., Itsweire, 1984;

470 Moum, 1996; Cimatoribus et al., 2014), with results from the method introduced for atmospheric data

471 by Ellison (1957). In this Appendix, such a comparison is done for weakly stratified waters. A

472 modification is proposed of the Ellison (1957) method for application to data from moored instrumented

473 strings, and which is practically based on instrument performance and environmental physics conditions.

474   Ellison (1957) separated time series of potential temperature $\theta(t, z)$, which is dynamically equivalent

475 to Conservative Temperature Θ (IOC et al., 2010) in the ocean, at a fixed vertical position z in two,

476     $\theta = <\theta> + \theta'$,   (A1)

477 where <.> denotes the lpf series and the prime its hpf equivalent. If multiple sensors are deployed in the

478 vertical to establish a mean vertical gradient, a scale height can be defined as,

479     $L_E = <\theta'^2>^{1/2}/(d<\theta>/dz)$.   (A2)

480   Itsweire (1984), using laboratory CTD-profile data, and Moum (1996), using ocean microstructure

481 profiler data, apply sorting as filter in z-direction. While their quasi-hpf data unlikely contain (linear)

482 internal waves, provided the profiles were instantaneously made and strictly vertical, they may contain

483 instrumental noise. With limited time-evolution available, it is assumed that the hpf data have worked

484 against the local stratification. The same assumption is made for Thorpe (1977) displacements. Sorting

485 works on all scales of overturns, which can be highly varying.

486   Like Thorpe-displacement 'd' scales, the Ellison scales of (A2) may be compared with the Ozmidov

487   (1965) scale $L_O = cL_E$ of largest possible turbulent overturns in stratified waters, so that the turbulence

488   dissipation rate reads,

489        $\varepsilon_E = c^2 L_E^2 N^3,$ (A3)

490   in which the constant c needs to be established. If we take an average value of c = 0.8 (Dillon, 1982),

491   like commonly used for vertical root-mean-square 'rms' Thorpe scale $L_T = [d^2]$ so that $\varepsilon_T = c^2 L_T^2 N^3$, one

492   can compare average dissipation rate values between the two methods.

493   While the Thorpe (1977) method is most sensitive to proper resolution of the largest vertical overturn

494   scale, and the stratification (or buoyancy frequency) it works against, determination of Ellison scales

495   from moored-sensor time series is most sensitive for the appropriate separation between internal waves

496   and turbulent motions (Cimatoribus et al., 2014). For data from instrumented strings under well-

497   stratified Northeast-Atlantic conditions, wavelet decomposition worked using an averaging scale of

498   about 2/N for the lpf in (A1). Under such conditions, instrumental flaws like short-term bias of T-sensor

499   data were minimal. However, such a determination of Ellison scales is not a straightforward task under

500   weakly stratified and near-homogeneous conditions like occurring in the deep Western Mediterranean.

501   First, because such conditions imply very small variations in temperature (density), time series

502   require lpf to remove instrumental noise.

503   Second, time series require hpf to remove internal waves and (sub-)mesoscale motions. While the

504   common internal-wave band is considered between ranges f and N, for well stratified waters N >> f,

505   more complex inertio-gravity wave 'IGW' frequency 'ω' bounds [$\omega_{min} < f, \omega_{max} > N$], for large-scale mean

506   N, have to be considered in waters where N = O(f), e.g. (LeBlond and Mysak, 1978; Gerkema et al.,

507   2008). Furthermore, while average large-scale stratification hampers turbulent overturns, internal-wave

508   straining separates small thin-layer stratification, with small-vertical-scale buoyancy frequency N_s, from

509   near-homogeneous layers, with minimum buoyancy frequency N_{min}, which may carry ditto waves

510   extending beyond the mean-N IGW-bounds. At the low-frequency, sub-inertial side of the IGW-band

511   the rare N_{min} may combine with sub-mesoscale motions. More importantly, at the high-frequency, super-

512   buoyancy side N_s may combine with turbulent overturns. If all relevant scales are resolved, a safe

513   separation frequency would thus be at overall maximum $N_{max} = max(max(N_s))$, where the maximum

514   between brackets is determined for each profile. In practice, such a transition frequency between internal

515   waves and turbulence is not easily determined, because it requires the small scales to resolve relevant

516   L_O. Only in weakly stratified waters, L_O are $O(10)$ m, and resolution of 1-2 m scales should be sufficient.

517   Thus, under weakly stratified conditions, instrumental noise and short-term bias have to be corrected

518   in t- and z-direction, respectively. A practical solution that also eliminates internal waves and sub-

519   mesoscale motions, is application of a band-pass filter 'bpf' in t, an lpf and sorting in z so that per time

520   step (A2) reads,

521        $|\theta'_{bpf}|/(d\theta_{sorted}/dz)$,

522   to which sufficient averaging is applied. Noting that stratification varies over different scales by two

523   orders of magnitude, so that $N_s \approx 0\text{-}6f$, filter design discriminates between conditions of SW and NH.

524   Sharp, phase-preserving double-elliptic filters (Parks and Burrus, 1987) are designed following

525   inspection of temperature variance spectra (Fig. A2).

526   For SW, reasonable filter cut-offs are tuned for a 1.7-day period around day 308 by equating (A3) to

527   ε_T. SW's lpf cut-off is fixed at 3000 cpd. The reference hpf cut-off frequency $\omega_{hpf,ref}$ appeared at a small

528   flat (0-)slope near the low end of turbulence buoyancy-($\omega^{-7/5}$) and inertial-subrange ($\omega^{-5/3}$) slopes, where

529   a short steep slope to internal-wave frequencies occurred. For other SW-periods, reference is not made

530   using average large-scale N, but a better fit is found for the time average of maximum small-scale

531   buoyancy frequencies per profile $N_m = \langle max(N_s) \rangle$ so that,

532        $\omega^{SW}_{hpf} = (N_m/N_{m,ref})^2 \omega_{hpf,ref}$.   (A4)

533   For NH, the lpf cut-off is fixed at 500 cpd. For its hpf cut-off, a flat (0-) slope appeared at a frequency

534   just higher than ω_{max} so that, independent of measured $\langle N_{s,max} \rangle$ the cut-off is blocked at,

535        $\omega^{NH}_{hpf} = 3.7$ cpd.   (A5)

536   This value is tuned for a period with dominant GH, for which the geophysics-determined (e.g., Pasquale

537   et al., 1996) buoyancy flux $fl/\Gamma_C = \varepsilon_{GH} = 1.2 \times 10^{-10}$ m^2 s^{-3}. In the present (Fig. 6) and previous (van Haren,

538   2025) data the mixing coefficient was found to amount $\Gamma_C = 0.5$, which is typical for convection

539   turbulence (Dalziel et al., 2008; Ng et al., 2016).

540   The cut-off frequency in (A5) is to within ±0.2 cpd equivalent to $1.8(2\Omega) \approx 1.8 <\omega_{max}> \approx 2<N_{s,max}>$

541    $\approx 0.5<U>/<L_T> = 0.5\omega_O$, for the deep Western Mediterranean site. Ω denotes the Earth rotation, and U

542   the waterflow speed. The Ozmidov (1965) frequency ω_O is a natural separator between internal waves

543   and stratified turbulence. It is unknown why the filter cut-off is close to half the Ozmidov frequency.

544   Also puzzling is the lack of correspondence between (A4) and ω_O, with the factor varying between 0.3

545   and 0.9 for different periods of SW. In part this may have to do with the waterflow being measured at h

546   = 126 m, below which it may be more uniform under NH- than under SW-conditions.

547   As shown in Fig. 4 for (A4), and Fig. 5 for (A5), the comparison works well to within about 20%.

548   For Fig. 4, $<[\varepsilon_T]> = 6.3 \times 10^{-10}$ m^2 s^{-3} and $<[\varepsilon_E]> = 6.7 \times 10^{-10}$ m^2 s^{-3}. For Fig. 5, $<[\varepsilon_T]> = 2.0 \times 10^{-10}$ m^2 s^{-3}

549   and $<[\varepsilon_E]> = 1.3 \times 10^{-10}$ m^2 s^{-3}. Further tests were performed for about ten 1-4 day periods of NH and

550   SW, and all were within above error, provided that the data post-processing was carefully done and

551   longer periods were avoided. Especially (A5) is very sensitive to small changes in filter steepness around

552   the cut-off frequency, presumably due to its proximity to the IGW upper bound.

553

554 **References**

555 Adrián-Martinez, S. et al.: Letter of intent for KM3NeT 2.0, J. Phys. G, 43, 084001, 2016.

556 Brainerd, K. E., and Gregg, M. C.: Surface mixed and mixing layer depths, Deep-Sea Res. I, 42, 1521-

557   1543, 1995.

558 Cimatoribus, A. A., van Haren, H., and Gostiaux, L.: Comparison of Ellison and Thorpe scales from

559   Eulerian ocean temperature observations, J. Geophys. Res., 119, 7047-7065, 2014.

560 Crepon, M., Wald, L., and Monget, J. M.: Low frequency waves in the Ligurian Sea during December

561   1977, J. Geophys. Res., 87, 595-600, 1982.

562 Dalziel, S. B., Patterson, M. D., Caulfield, C. P., and Coomaraswamy, I .A.: Mixing efficiency in high-

563   aspect-ratio Rayleigh-Taylor experiments, Phys. Fluids, 20, 065106, 2008.

564 Dickson, R. R., Lazier, J. R. N., Meincke, J., Rhines, P., and Swift, J.: Longterm coordinated changes

565   in the convective activity of the North Atlantic, Progr. Oceanogr., 38, 241-295, 1996.

566 Dillon, T. M.: Vertical overturns: a comparison of Thorpe and Ozmidov length scales, J. Geophys. Res.

567   87, 9601-9613, 1982.

568 Ellison, T. H., Turbulent transport of heat and momentum from an infinite rough plane, J. Fluid Mech.,

569   2, 456-466, 1957.

570 Eriksen, C. C.: Observations of internal wave refection of sloping bottoms, J. Geophys. Res., 87, 525-

571   538, 1982.

572 Ferron, B., Bouruet Aubertot, P., Cuypers, Y., Schroeder, K., and Borghini, M.: How important are

573   diapycnal mixing and geothermal heating for the deep circulation of the Western

574   Mediterranean? Geophys. Res. Lett., 44, 7845-7854, 2017.

575 Gerkema, T., Zimmerman, J. T. F., Maas, L. R. M., and van Haren, H.: Geological and astrophysical

576   fluid dynamics beyond the traditional approximation, Rev. Geophys., 46, RG2004, 2008.

577 Gregg, M. C.: Scaling turbulent dissipation in the thermocline, J. Geophys. Res., 94, 9686-9698, 1989.

578 IOC, SCOR, and IAPSO: The International Thermodynamic Equation of Seawater – 2010: Calculation

579   and Use of Thermodynamic Properties, Intergovernmental Oceanographic Commission,

580   Manuals and Guides No. 56, UNESCO, Paris, 196 pp, 2010.

581   Itsweire, E. C.: Measurements of vertical overturns in a stably stratified turbulent flow, Phys. Fluids,

582   27, 764-766, 1984.

583   Kunath, P., Chi, W.-C., Berndt, C., and Liu, C.-S.: A rapid numerical method to constrain 2D focused

584   fluid flow rates along convergent margins using dense BSR-based temperature field data, J.

585   Geol. Res. Solid Earth, 126, e2021JB021668, 2021.

586   LeBlond, P. H., and Mysak, L. A.: Waves in the Ocean, Elsevier, New York, 602 pp, 1978.

587   Lilly, J. M., Rhines, P. B., Visbeck, M., Davis, R., Lazier, J. R. N., Schott, F., and Farmer, D.: Observing

588   Deep Convection in the Labrador Sea during Winter 1994/95, J. Phys. Oceanogr., 29, 2065-

589   2098, 1999.

590   Marshall, J., and Schott, F.: Open-ocean convection: Observations, theory, and models, Rev. Geophys.

591   37, 1-64, 1999.

592   McEwan, A. D.: A laboratory demonstration of angular momentum mixing, Geophys. Fluid Dyn., 5,

593   283-311, 1973.

594   Mertens, C., and Schott, F.: Interannual Variability of Deep-Water Formation in the Northwestern

595   Mediterranean, J. Phys. Oceanogr., 28, 1410-1424, 1998.

596   Moum, J. N.: Energy-containing scales of turbulence in the ocean thermocline, J. Geophys. Res., 101,

597   14,095-14,109, 1996.

598   Ng, C. S., Ooi, A., and Chung, D.: Potential energy in vertical natural convection, Proc. 20th

599   Australasian Fluid Mech. Conf., Paper 727, 4 pp.,

600   https://people.eng.unimelb.edu.au/imarusic/proceedings/20/727 Paper.pdf, 2016.

601   Oakey, N. S.: Determination of the rate of dissipation of turbulent energy from simultaneous temperature

602   and velocity shear microstructure measurements, J. Phys. Oceanogr., 12, 256-271, 1982.

603   Osborn, T. R.: Estimates of the local rate of vertical diffusion from dissipation measurements, J. Phys.

604   Oceanogr. 10, 83-89, 1980.

605   Ozmidov, R. V.: About some peculiarities of the energy spectrum of oceanic turbulence, Dokl. Akad.

606   Nauk SSSR, 161, 828-831, 1965.

607   Parks, T. W., and Burrus, C. S.: Digital Filter Design, John Wiley Sons, New York, 342 pp, 1987.

608   Pasquale, V., Verdoya, M., and Chiozzi, P.: Heat flux and timing of the drifting stage in the Ligurian–
609   Provençal basin (northwestern Mediterranean), J. Geodyn., 21, 205-222, 1996.

610   Polzin, K. L., Toole, J. M., Ledwell, J. R., and Schmitt, R. W.: Spatial variability of turbulent mixing in
611   the abyssal ocean, Science, 276, 93-96, 1997.

612   Schott, F., Visbeck, M., Send, U., Fischer, J., Stramma, L., and Desaubies, Y.: Observations of deep
613   convection in the Gulf of Lions, northern Mediterranean, during the winter of 1991/ 92, J. Phys.
614   Oceanogr., 26, 505-524, 1996.

615   Sheremet, V. A.: Laboratory experiments with tilted convective plumes on a centrifuge: A finite angle
616   between the buoyancy force and the axis of rotation, J. Fluid Mech., 506, 217-244, 2004.

617   Steffen, E. L., and D'Asaro, E.: Deep convection in the Labrador Sea as observed by Lagrangian floats,
618   J. Phys. Oceanogr., 32, 475-492, 2002.

619   Straneo, F., Kawase, M., and Riser, S. C.: Idealized models of slantwise convection in a baroclinic flow,
620   J. Phys. Oceanogr., 32, 558-572, 2002.

621   Thorpe, S. A.: Turbulence and mixing in a Scottish loch, Phil. Trans. Roy. Soc. Lond. A, 286, 125-181,
622   1977.

623   Thorpe, S. A.: Current and temperature variability on the continental slope, Phil. Trans. Roy. Sot. Lond.
624   A, 323, 471-517, 1987.

625   Thorpe, S. A.: The turbulent ocean, Cambridge Univ Press, Cambridge, 439 pp, 2005.

626   van Haren, H.: Abrupt transitions between gyroscopic and internal gravity waves: the mid-latitude case,
627   J. Fluid Mech., 598, 67-80, 2008.

628   van Haren, H.: Philosophy and application of high-resolution temperature sensors for stratified waters,
629   Sensors, 18, 3184, doi:10.3390/s18103184, 2018.

630   van Haren, H.: Thermistor string corrections in data from very weakly stratified deep-ocean waters,
631   Deep-Sea Res. I, 189, 103870, 2022.

632   van Haren, H.: Corrected values of turbulence generated by general geothermal convection in deep
633   Mediterranean waters, Ocean Dyn., 75, 46, 2025.

634   van Haren, H., and Dijkstra, H. A.: Convection under internal waves in an alpine lake, Env. Fluid Mech.,
635   21, 305-316, 2021.

636   van Haren, H. and Gostiaux, L.: Detailed internal wave mixing observed above a deep-ocean slope, J.

637   Mar. Res., 70, 173-197, 2012.

638   van Haren, H., and Millot, C.: Seasonality of internal gravity waves kinetic energy spectra in the

639   Ligurian Basin, Oceanol. Acta, 26, 635-644, 2003.

640   van Haren, H., Bakker, R., Witte, Y., Laan, M., and van Heerwaarden, J.: Half a cubic hectometer

641   mooring-array 3D-T of 3000 temperature sensors in the deep sea, J. Atmos. Ocean. Technol.,

642   38, 1585-1597, 2021.

643   van Haren, H., et al.: Whipped and mixed warm clouds in the deep sea, Geophys. Res. Lett., in press,

644   2026.

645   Yasuda, I., et al.: Estimate of turbulent energy dissipation rate using free‑fall and CTD‑attached

646   fast‑response thermistors in weak ocean turbulence, J. Oceanogr., 77, 17-28, 2021.

647

648 **Table 1.** General first and second moment statistics calculated for 45-line, 124-m height, and half-day

649 period turbulence dissipation rate values of Fig. 6. Two environmental conditions are characterized:

650 SW = stratified-water, NH = near-homogenous, and may include GH. The two conditions are

651 separated by a criterion equivalent of N = 0.65f.

652

Day	ε_T [m^2 s^{-3}]	Cond.
308	$4.0 \pm 0.8 \times 10^{-10}$	SW
441	$1.5 \pm 0.1 \times 10^{-9}$	SW
459	$1.0 \pm 0.2 \times 10^{-10}$	NH
495	$1.0 \pm 0.2 \times 10^{-10}$	NH
485	$4.8 \pm 0.4 \times 10^{-10}$	SW
652	$1.4 \pm 0.1 \times 10^{-10}$	NH
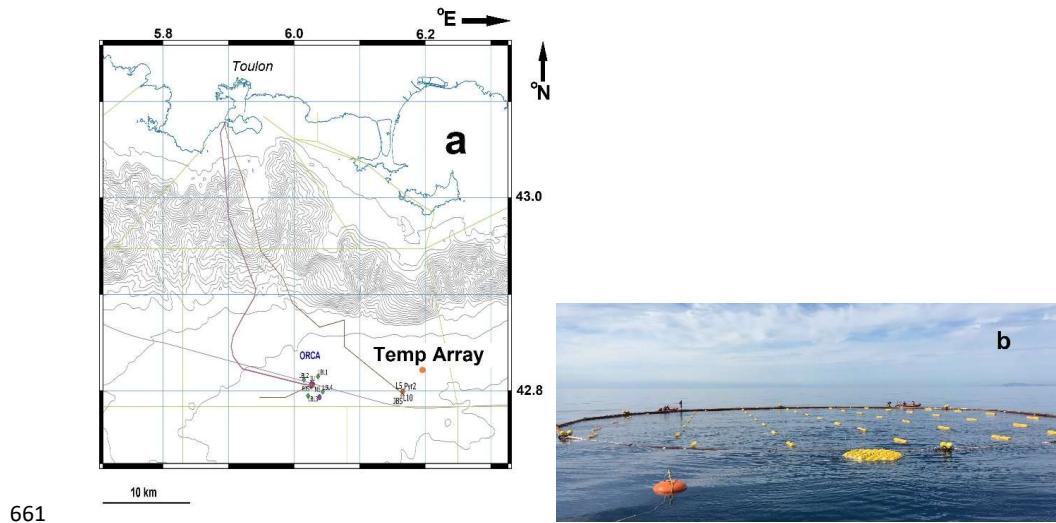
Figure 1. Large-ring mooring site and deployment. (a) Location named "Temp Array" (orange dot) on map off southern France. The mooring is well east of main neutrino telescope 'NT' site "ORCA" of KM3NeT (Adrián-Martinez et al., 2016) and just northeast of the former ANTARES NT-site. Isobaths are drawn every 100 m. (b) At sea, during deployment finalizing the opening of air valves before sinking. The near part of the large steel-tube ring is already underwater. Almost all buoys of the 45 small-ring compacted vertical lines are visible (for layout see Appendix A1).
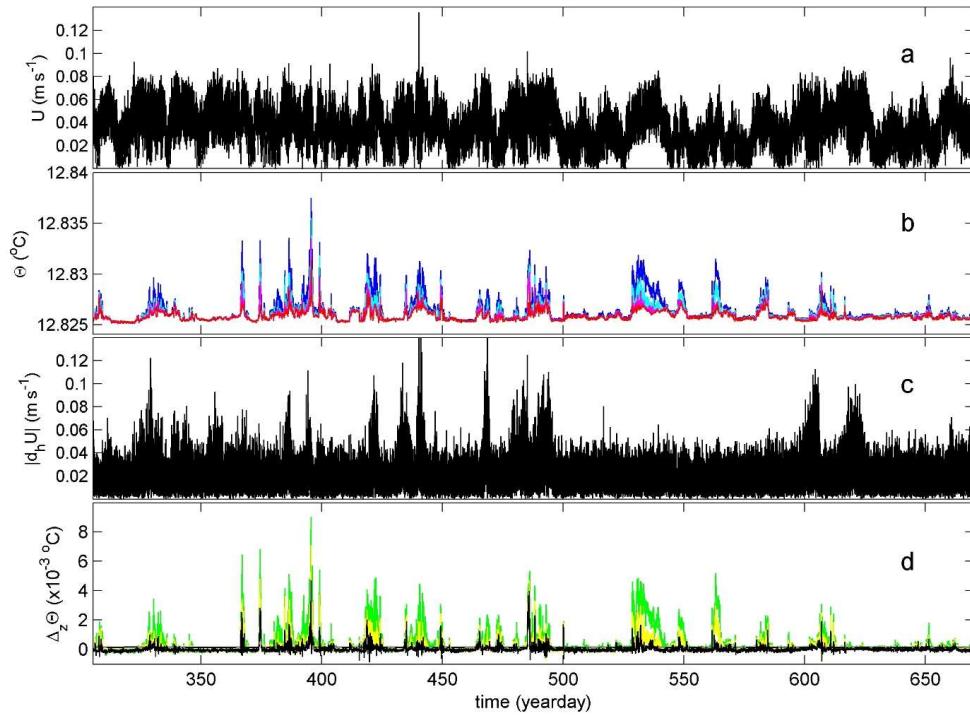
669
670   **Figure 2.** Time series of T-sensor and current meter 'CM' data, for the first year after deployment. Time

671   in days of year 2020, +366 in 2021. (a) Unfiltered waterflow speed at h = 126 m above seafloor. (b)

672   Conservative Temperature from vertical line 25, at h = 1.5 (red), 29.5 (magenta), 59.5 (cyan) and

673   99.5 m (blue), corrected for drift and referenced to CTD-data of Fig. 3b. (c) Amplitude of horizontal

674   flow differences. (d) Vertical temperature differences between the lowest T-sensor and those above

675   from b.
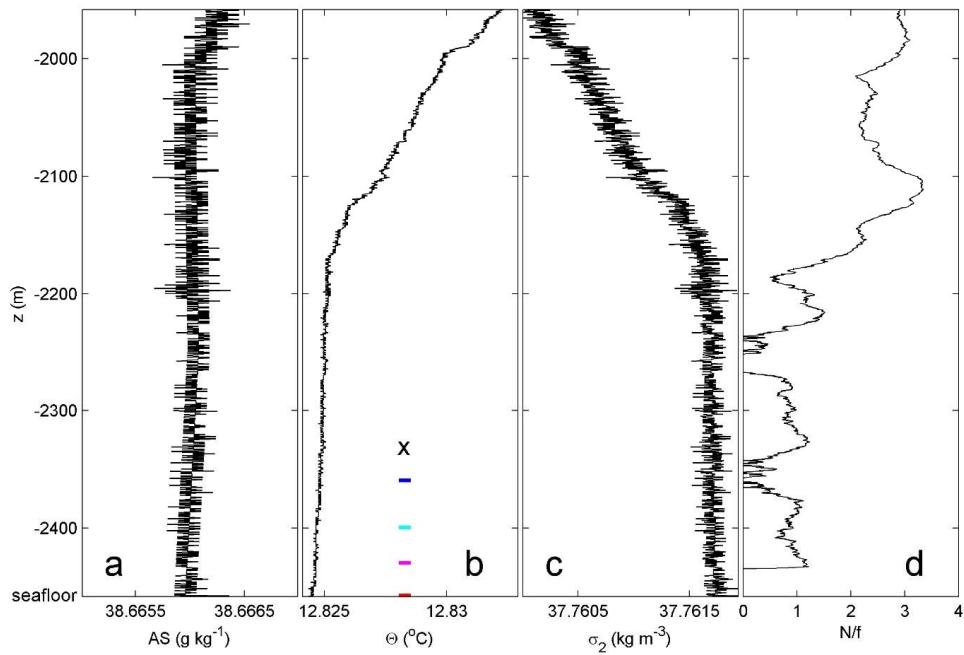
Figure 3. Lower 500 m of shipborne CTD profile obtained to within 0.5 m from the seafloor (at z = -2458 m). (a) Absolute Salinity, with x-axis range similar to that of b. in terms of contribution to density variations. (b) Conservative Temperature. The colored ticks indicate the vertical positions of the four T-sensors of which data are displayed in Fig. 2a. The 'x' indicates the position of CM. (c) Density anomaly referenced to 2×10^7 N m^{-2}. (d) Ratio of 25-m scale buoyancy frequency 'N' over local inertial frequency 'f'.
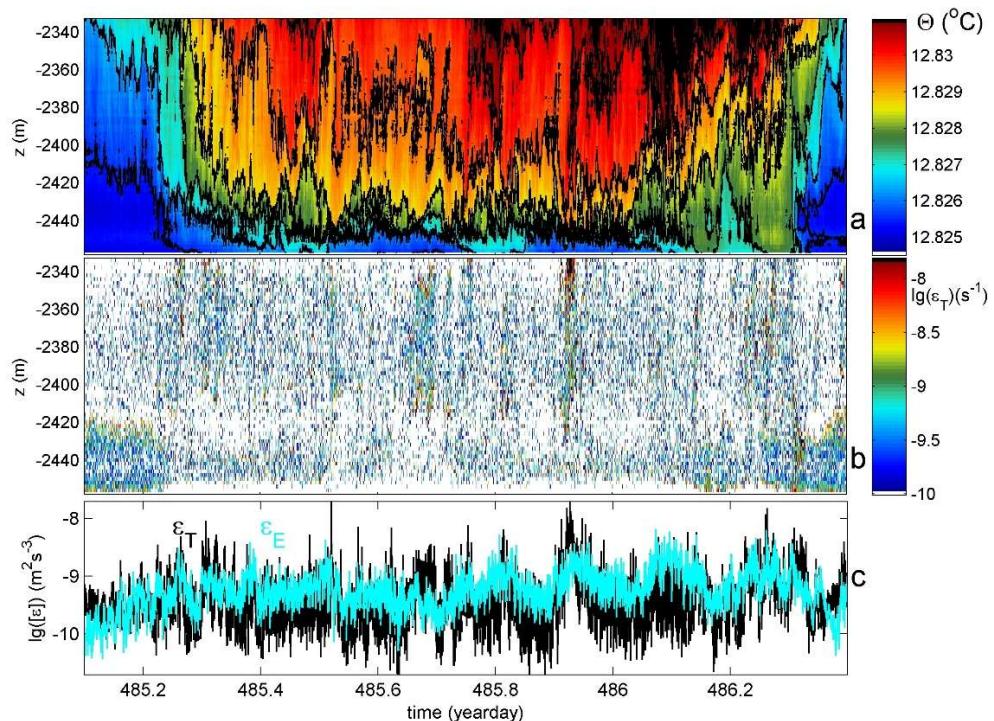
684
685 **Figure 4**. A 1.3-day period of relatively strong stratification with maximum small-scale buoyancy

686 frequency $N_{max} = 6f$, for data from vertical line 15. (a) Time-depth plot of Conservative Temperature

687 with black contours every 0.001°C. The horizontal axis is at the seafloor. (b) Logarithm of non-averaged

688 turbulence dissipation rate from data in a. using Thorpe (1977) method. (c) Time series of logarithm of

689 data from b. averaged over 124-m vertical extent of T-sensors (black), compared with calculations using

690 Ellison (1957) method (cyan) with high-pass filter 'hpf' cut-off from Fig. A2a.

691

692
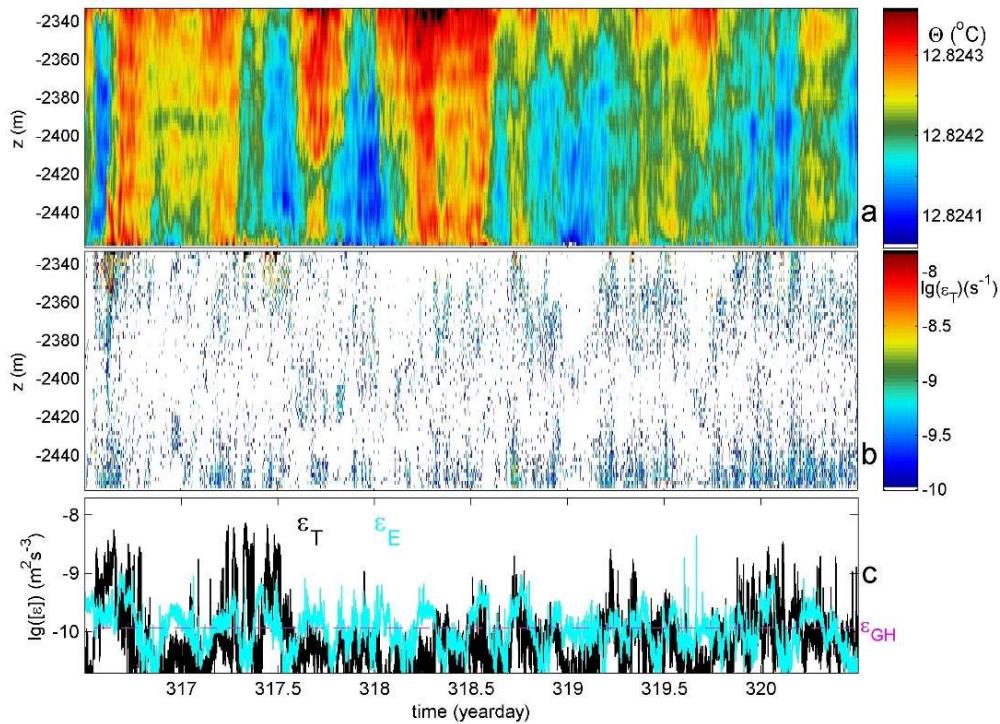
Figure 5. As Fig. 4, but for four days of near-homogeneous conditions with mean $N \approx 0.5f$, very weak

stratification alternated with convectively unstable periods. For c., the hpf cut-off for determining ε_E is

shown in Fig. A2b and the magenta-dashed line indicates the average dissipation rate attributed to

geothermal heating 'GH' (see text).
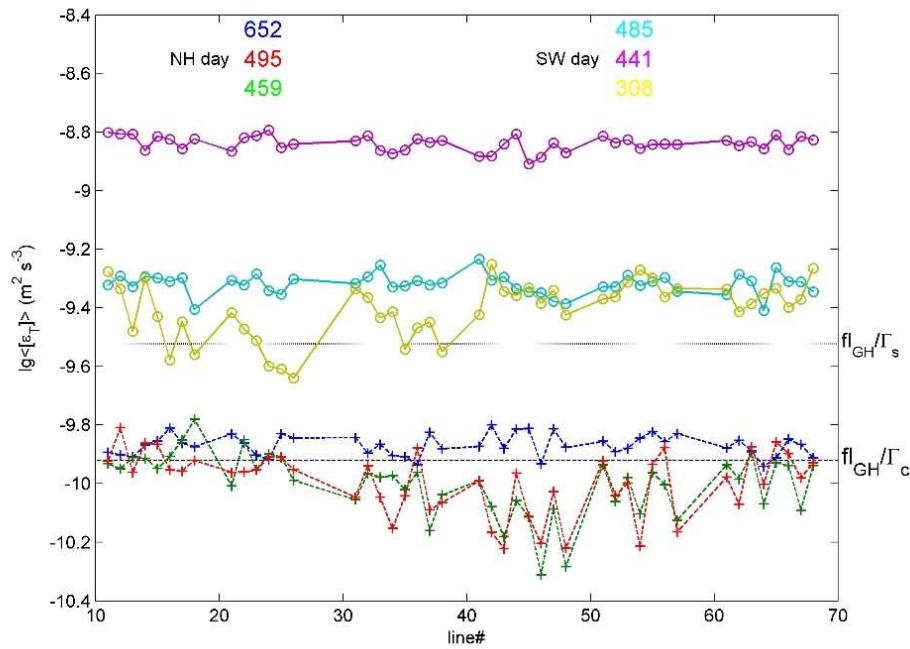
Figure 6. Limited statistics of Thorpe (1977) method (logarithm of) turbulence dissipation rates averaged over 124 m vertically given for six 12-h periods indicated by day-number, as a function of all 45 lines that are indicated their number 'line#'. Two thresholds are given as a function of general average buoyancy flux 'fl' from GH, divided by mixing coefficient for convection-turbulence $\Gamma_c = 0.5$ (Dalziel et al., 2008) and for shear-turbulence $\Gamma_S = 0.2$ (Osborn, 1980; Oakey, 1982). Solid lines (o) indicate Stratified-Water 'SW' conditions, dashed lines (+) indicate near-homogeneous 'NH' conditions.
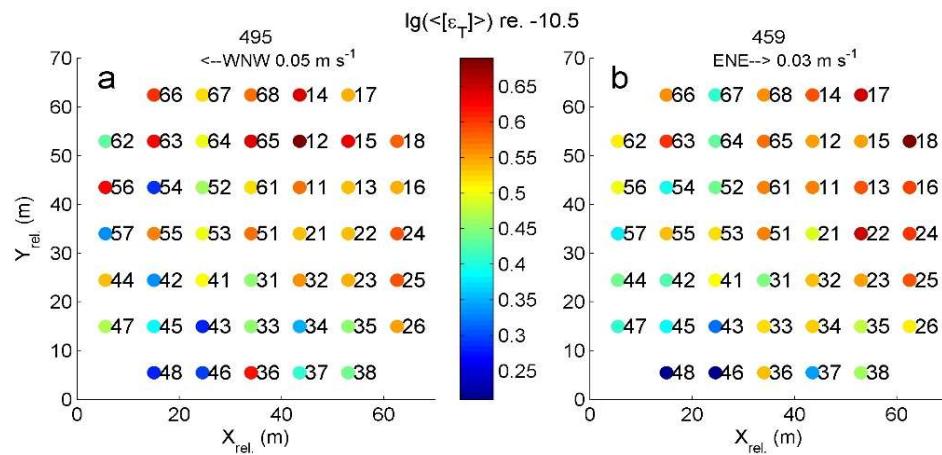
706
Figure 7. Plan view of 4 lines indicating logarithm relative to a value of -10.5 of time- and vertical-mean

708 turbulence dissipation rates for NH conditions on days 459 and 495 of Fig. 6. On top, half-day mean

709 waterflows are indicated.

710

711
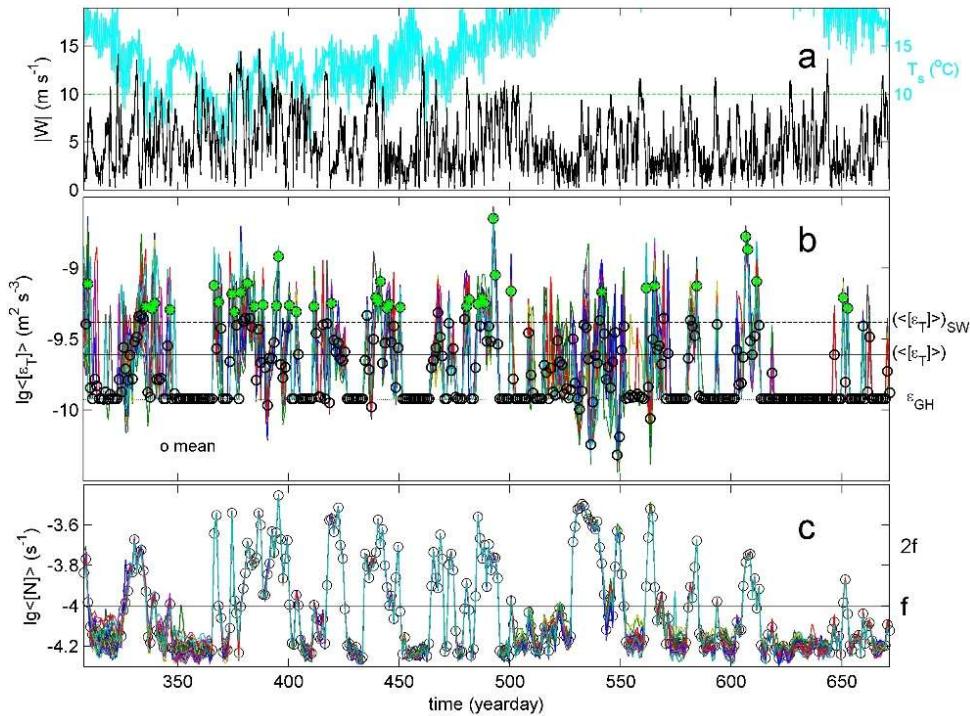
Figure 8. Yearlong time series of 45-line, daily, and vertically averaged turbulence and stratification values

compared with meteorological data. (a) Wind speed (black) and surface temperature (cyan) measured at

the station of Porquerolles Island, 20 km north of the mooring-array. The horizontal line is an arbitrary

reference line below which near-surface convection may occur under sufficient pre-conditioning. (b)

Logarithm of daily and 124-m vertically averaged Thorpe (1977) method turbulence dissipation rate for

all 45 lines (colour), including their mean values (black, circles) of which those exceeding twice the

overall mean value (green asterisks). A threshold of 0.0002°C is applied for T(125)-T(1), below which

values are forced to mean $\varepsilon_{GH} = 1.2 \times 10^{-10}$ m^2 s^{-3}, see text. The solid horizontal line indicates the overall

mean value (4), the dashed line the mean (5) for periods under SW conditions. (c) Logarithm of

corresponding mean buoyancy frequencies from reordered temperature profiles. The horizontal line

indicates the local planetary inertial frequency.
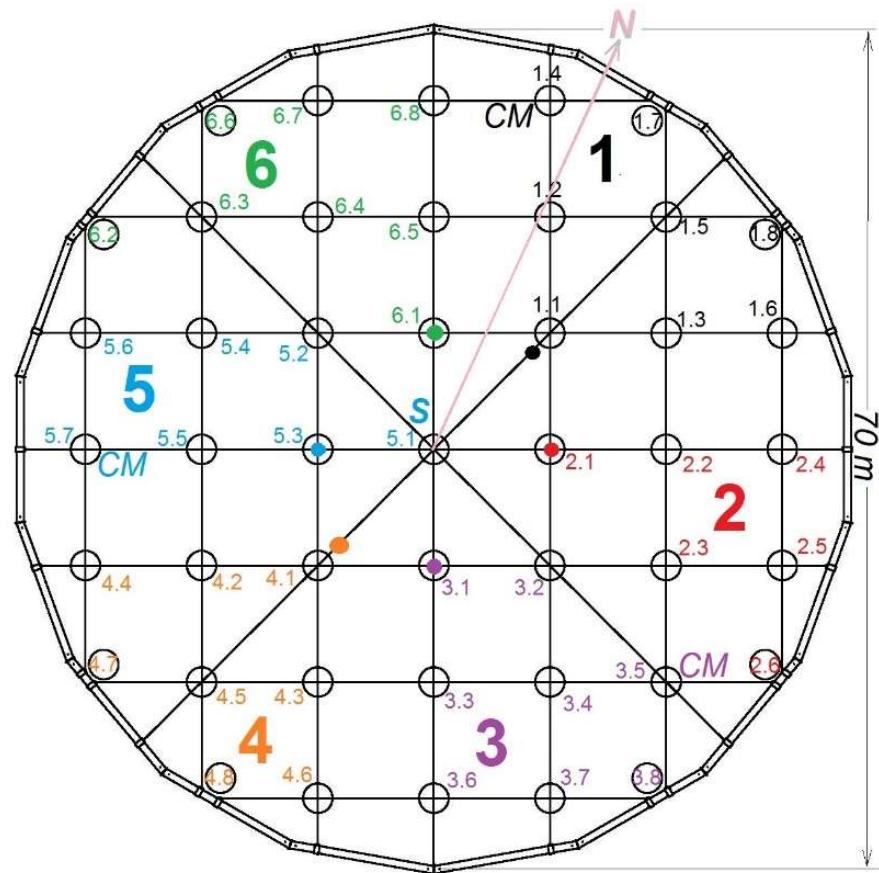
Figure A1. Orientation and layout of the large-ring mooring, with steel-cable grid and small rings numbered

in six synchronisation groups with colour dots indicating group nodes and synchronier 'S' at line 51.

Here and elsewhere in the text, lines are indicated without period for short. Lines 14, 35 and 57 held a

waterflow current meter 'CM' at the buoy.
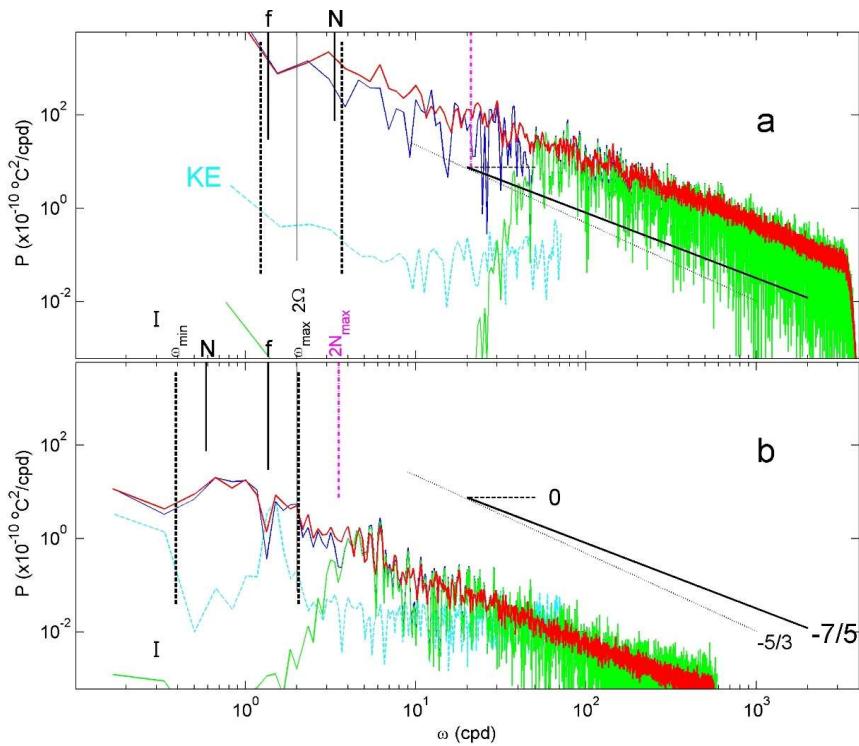
Figure A2. Spectra demonstrating filter cut-off frequencies for Ellison (1957) method under SW and NH
conditions. Data from line 15. Weakly smoothed (6 degreed of freedom, dof) low-pass filtered 'lpf'
spectra from a single T-sensor at mid-height (blue) with hpf version (green) is compared with
moderately smoothed (100-dof) lpf spectrum over all 63 T-sensors (red). For comparison, the weakly
smoothed (10-dof) kinetic energy 'KE' spectra are given (cyan; arbitrary vertical scale), averaged over
the three CM. For reference, several frequencies and turbulence-range spectral slopes are given, see
text. (a) SW period of Fig. 4, with filter cut-off following a scaling of time mean $<N_{max}>^2$ and lpf cut-
off at 3000 cpd (cycles per day). (b) NH period of Fig. 5, with hpf cut-off fixed near $2<N_{max}>$ and lpf
cut-off at 500 cpd.